Unveiling the Electro-Chemo-Mechanical Failure Mechanism of Sodium Metal Anodes in Sodium-Oxygen Batteries by Synchrotron X-ray Computed Tomography

Xia Zhang [+], Shenghang Zhang [+], Jie Lu, Fengcheng Tang, Kang Dong, Zhenjiang Yu, André Hilger, Markus Osenberg, Henning Markötter, Fabian Wilde, Shu Zhang, Jingwen Zhao, Gaojie Xu, Ingo Manke, Fu Sun,* and Guanglei Cui*

Xia Zhang, Shenghang Zhang, Jie Lu, Fengcheng Tang, Shu Zhang, Jingwen Zhao,Gaojie Xu, Fu Sun, Guanglei Cui

Qingdao Institute of Bioenergy and Bioprocess Technology Chinese Academy of Sciences, 266101 Qingdao, Shandong, China

Shandong Energy Institute, Qingdao 266101, China

Qingdao New Energy Shandong Laboratory, Qingdao 266101, China

Kang Dong, André Hilger, Markus Osenberg, Ingo Manke

Helmholtz-Zentrum Berlin für Materialien und Energie

Hahn-Meitner-Platz 1, 14109 Berlin, Germany

Zhenjiang Yu

Department of Chemistry, Lancaster University

Lancaster LA1 4YB, United Kingdom

Henning Markötter

Bundesanstalt für Materialforschung und -prüfung

Unter den Eichen 87, 12205 Berlin, Germany

Fabian Wilde

Institute of Materials Physics, Helmholtz-Zentrum Hereon, Max-Planck-Straße 1, 21502 Geesthacht, Germany

Xia Zhang's Present address:

Helmholtz-Zentrum Berlin für Materialien und Energie

Hahn-Meitner-Platz 1, 14109 Berlin, Germany

Abstract

Rechargeable sodium-oxygen batteries (NaOBs) are receiving extensive research interests because of their advantages such as ultrahigh energy density and cost efficiency. However, the severe failure of Na metal anodes has impeded the commercial development of NaOBs. Herein, combining *in-situ* synchrotron X-ray computed tomography (SXCT) and other complementary characterizations, a novel electro-chemo-mechanical failure mechanism of sodium metal anode in NaOBs is elucidated. It is visually showcased that the Na metal anodes involve a three-stage decay evolution of a porous Na reactive interphase layer (NRIL): from the initially dot-shaped voids evolved into the spindle-shaped voids and the eventually-developed ruptured cracks. The initiation of this three-stage evolution begins with chemical-resting and is exacerbated by further electrochemical cycling. From corrosion science and fracture mechanics, theoretical simulations suggest that the evolution of porous NRIL is driven by the concentrated stress at crack tips. Our findings illustrate the importance of preventing electro-chemo-mechanical degradation of Na anodes in practically rechargeable NaOBs.

1. Introduction

Rechargeable alkali metal-O_2 batteries are attracting a surging interest as promising power batteries for electric vehicles owing to their extremely high theoretical energy density that is comparable with gasoline.[1-6] Intense attention has been concentrated on aprotic lithium-O_2 battery (LiOB, 3485 Wh kg^{-1} for Li_2O_2) technology since its introduction in 1996 by Abraham.[7] Nevertheless, considerable challenges such as high overpotential, low Coulombic efficiency and limited Li resources have fundamentally hindered the successful implementation of LiOBs.[8-9] In comparison, the sodium-O_2 battery (NaOB) technology, despite its relatively lower theoretical specific energy (1602 Wh kg^{-1} for Na_2O_2), seems to be a competitive candidate because of its lower overpotential (< 200 mV) and higher round-trip efficiency.[10-15] Moreover, sodium is the fourth most abundant element on the earth, rendering it one of the most cost-

effective electrode materials.[16-18] Thus, NaOB is expected to be one of the most promising next-generation battery technologies that can be extensively deployed due to high energy-density and low-cost Na anodes. However, the NaOB technology is currently in its infancy stage and the hitherto reported battery performance is unable to compete with the current lithium-ion battery technology.[19-21] The fundamental cause for the inferior performances of NaOB technology can be ascribed to an inadequate and incomprehensive understanding of the working principles and failure mechanisms.[22]

Significant efforts have been devoted to address this issue and in-depth understanding has been achieved. Velinkar et al. found that the energy dynamics during discharge and charge processes at carbon/electrolyte interfaces in NaOBs, which are influenced by surface-mediated discharge, varied with the type of carbon cathode utilized.[4] It is demonstrated by Ortiz-Vitoriano et al. that the synergistic effects between diethylene glycol dimethyl ether (diglyme) and pyrrolidinium-based ionic liquid solvents can improve the superoxide anion stability and facilitate the uniform formation of NaO_2 crystals across the carbon cathode.[23] These reports underline the importance of choosing suitable cathode materials and electrolytes for NaOBs. However, the crucial role of Na metal anode in NaOBs has been seldomly explored.[24-25] Metallic Na has a redox potential of 0.34 V versus Li^+/Li, which is generally lower than the reduction potential of the most used electrolytes.[26] For example, the tetraglyme based electrolyte is susceptible to decompose after contacting Na anode.[27] In another study, Guo et al. photographically found that the surface of Na anode become rough and holey with increasing discharge depth, accelerating the parasitic reactions occurred on Na anode.[28] Furthermore, Na anode always suffer from uncontrollable Na dendrites growth and volume expansion, resulting in internal short-circuits and severe safety concerns of NaOBs.[29-32] These studies suggest that the severe failure of Na anode also accelerates the capacity decay of NaOBs. Therefore, elucidating fundamental failure mechanisms of Na anode is very important in clarifying the reason for capacity decay of NaOBs, and will guide the engineering strategies for performance enhancement of NaOBs.

Considering the high chemical-reactivity and air-sensitivity of metallic Na, *in-situ*

characterization technique that is capable of probing the failure evolution processes of Na anodes non-destructively during the charge-discharge processes is highly required. *In-situ* spectroscopy tools, such as nuclear magnetic resonance, Raman spectroscopy, Fourier transform infrared spectroscopy etc., have been used to characterize the growth of Na dendrites and the associated solid electrolyte interface,[33-34] yet these probing techniques can hardly present the morphological changes of the evolved Na anodes, which are closely related to the physicochemical phenomena that straightforwardly dictate their performance.[35] Although the *in-situ* light microscopy and electron microscopy have been frequently used to reveal the morphological evolution of Na anodes during battery cycling,[36-37] their intrinsic two-dimensional (2D) results suffer from the inability to comprehensively illustrate the complexity of the inherently three-dimensional (3D) Na anodes. Hence, advanced *in-situ* analytical tools that are capable of providing direct visualization of the expansion/contraction and the crack or porosity evolution of the cycled Na anodes in 3D are highly desirable. Synchrotron X-ray computed tomography (SXCT) is a non-destructive imaging technique that uses X-rays to capture multiple projections from various angles to reconstruct a detailed 3D image of the internal structure of a material. In recent years, it is successfully validated that *in-situ* SXCT method is capable of non-destructively probing the local, even buried structures in varied battery systems, providing a great deal of unprecedented information from electrode surface to bulk.[38-45] Moreover, the 3D SXCT technique has been also used to study how the battery performance is influenced by the intrinsic properties of electrode materials such as porosities, microcracks, and the chemo-mechanical couplings.[46-48] To the best of our knowledge, there is still no report of using SXCT technique to non-destructively clarify failure evolution processes of Na anode in NaOBs.

In this work, the dynamic failure evolution of Na metal anode and its correlation to NaOBs performance degradation are systematically studied by *in-situ* SXCT technique, together with electrode/electrolyte interface characterizations and finite element analysis (FEA) methods. The *in-situ* SXCT technique clearly reveals that the decay of

NaOBs involves a three-stage evolution of a porous Na reactive interphase layer (NRIL) at Na metal anode: the initially formed dot-shaped voids (stage I) evolve into the spindle-shaped voids (stage II) and eventually into ruptured cracks (stage III). It is revealed by depth-profiling X-ray photoelectron spectroscopy (XPS) and time-of-flight secondary ion mass spectrometry (TOF-SIMS) characterizations that O_2 plays a crucial role in facilitating the reaction between Na metal and the electrolyte, leading to the thickening and cracking of the NRIL. The detailed three-stage evolution of the porous NRIL are discussed in context of corrosion science (pitting corrosion and stress corrosion cracking) and fracture mechanics. Furthermore, FEA simulations suggest that the mechanical stress concentrated at the cracks tip plays a significant role in driving their further propagation. To sum up, the current discoveries have provided coupled electro-chemo-mechanical insights into the failure mechanisms of Na anode in NaOBs during electrochemical cycling and these invaluable insights may bring forth fundamental breakthroughs for their practical applications.

2. Results and Discussion

Two types of NaOB design are used: the customized cell for *in-situ* SXCT (Figure S1, tomo-cell) and the commercialized Swagelok cell for postmortem characterizations (Figure S2a), Swagelok-cell). An illustration and a photograph of the tomo-cell are displayed in Figure S1a,b, the design of which has already been proved to be compatible with *in-situ* SXCT technique (Figure S1c).[49-50] All investigated NaOBs adopt sodium metal foil as anode, 1 M sodium triflate ($NaCF_3SO_3$) in diglyme as electrolyte and carbon fiber paper as cathode. Further experimental details are shown in the experimental section.

2.1 *Formation and three-stage evolution of the Na reactive interphase layer (NRIL)*

The degradation mechanisms of Na metal anodes in NaOBs are revealed by comparing their states before and after electrochemical cycling using the non-destructive *in-situ* SXCT technique. An uncycled tomo-cell (named **No. 0** tomo-cell), which serves as a reference to the cycled ones, is investigated by a laboratory X-ray facility and the result

is exhibited in Figure S2b,c. Four other cells (hereafter named **No. 1-No. 4** tomo-cell) cycled after different total capacities (different cycles) are further investigated by *in-situ* SXCT facility (Figure 1a1-d1). The captured internal changes of these cycled NaOBs viewed along the transversal x-z planes are shown in Figure 1a2-d2. From these images, one can clearly distinguish the Na metal anode, the glass fiber separator, and the carbon paper cathode. Compare these results with those from the pristine No. 0 tomo-cell (Figure S2b,c) and one can recognize the noticeable morphological changes of Na anodes after repeated Na electrodeposition and dissolution, especially the formation and three-stage evolution of a Na reactive interphase layer (NRIL). To be more specific, one can note that a NRIL of thickness of ~102 μm is generated after cycling the NaOBs (No. 1 tomo-cell) for 3.850 mAh cm^{-2}, as shown in Figure 1a2. The thickness of NRIL rises to ~174 and ~352 μm (Figure 1b2,c2) after increasing the areal capacity respectively to 7.844 mAh cm^{-2} (No. 2 tomo-cell) and 8.557 mAh cm^{-2} (No. 3 tomo-cell), respectively. After the NaOB is further cycled for 14.120 mAh cm^{-2} (No. 4 tomo-cell), it seems that its pristine bulk Na has transformed entirely into the NRIL, with notably huge and jagged cracks (Figure 1d2). The zoom-in views of the generated NRIL regions are further showcased in Figure 1a3-d3, from which, conspicuous darker regions (e.g., along the yellow double-headed lines) than the other regions are notable.[49, 51-52]

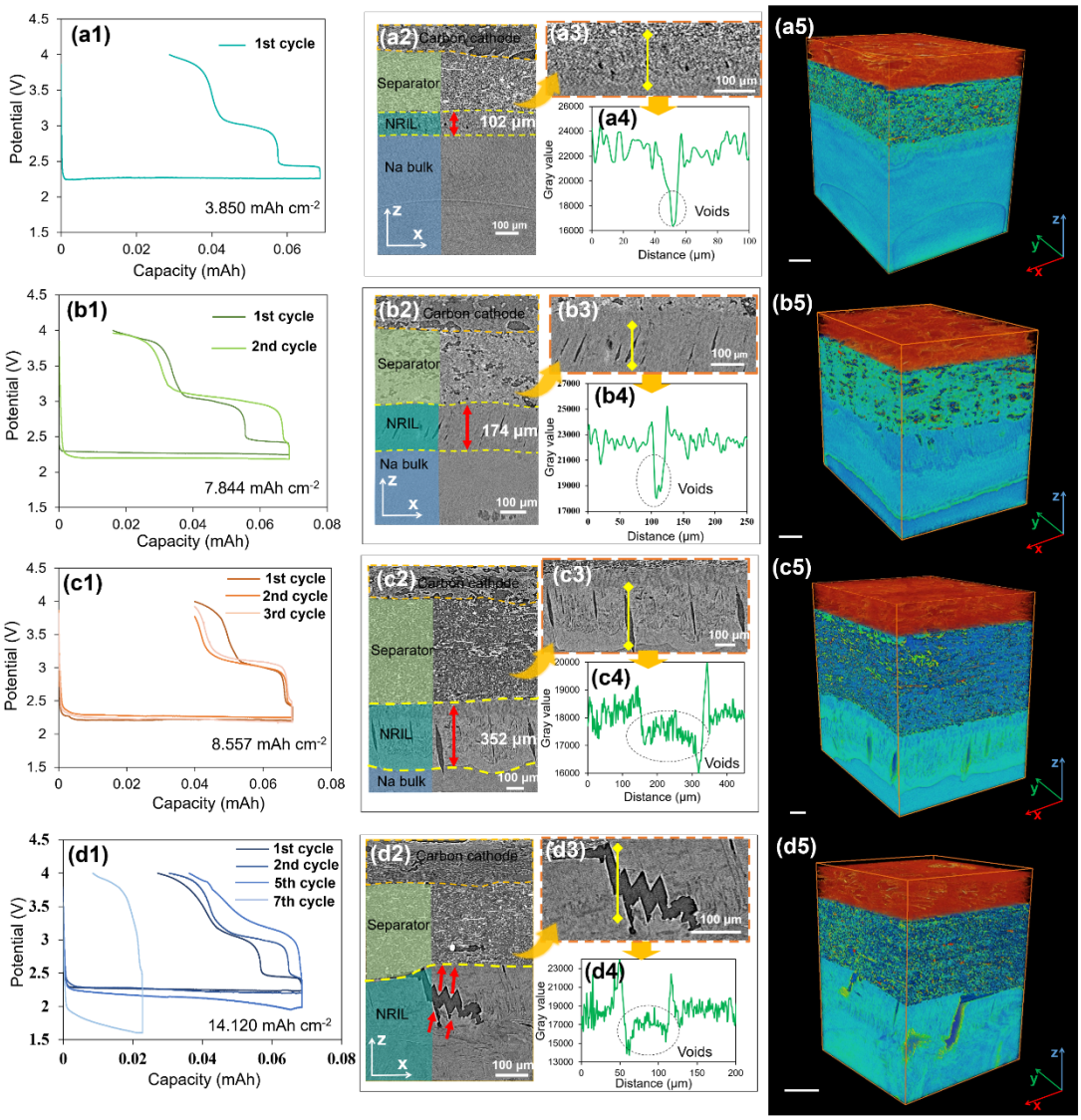

Figure 1. Electrochemical performance and microstructure evolution in the cycled NaOBs (No.1-4 tomo-cells). Electrochemical curves of the as-characterized cells after cycling at the capacity of 3.850 mAh cm^{-2} (a1), 7.844 mAh cm^{-2} (b1), 8.557 mAh cm^{-2} (c1) and 14.120 mAh cm^{-2} (d1). (a2-d2) Slices in the x-z plane taken from the reconstructed tomographic data. (a3-d3) The corresponding zoomed-in images of the NRIL. The yellow double-headed lines denote the lines along which the X-ray absorption coefficients are analyzed. (a4-d4) The line profiles along the yellow double-headed lines shown in a3-d3. (a5-d5) The corresponding 3D representations of the reconstructed data. All the scale bars are 100 μm.

According to the Beer-Lambert law, these dark areas have a relatively low X-ray absorption coefficient and thus a high X-ray transmittance capability and they are expected to be newly formed voids/cracks.[44, 45] This is confirmed by analyzing the X-ray absorption coefficients along the yellow lines shown in Figure 1a3-d3: as the analysis results in Figure 1a4-d4 imply a sudden decrease of the grayscale values at the

positions where these voids/cracks transect is obvious. However, it is worthy to note that these formed voids/cracks are highly likely refilled with the employed electrolyte although this is not certain due to its very low X-ray absorption coefficient.[51]

To further visualize the evolution of Na anode and the NRIL from different perspectives, the horizontal views along x-y plane and the 3D volume renderings of the reconstructed tomography data of No. 1-4 cells are analyzed, as shown respectively in Figure S3 and Figure 1a5-d5. From the result of No. 1 tomo-cell, one can note that some dark dotted voids appear within the NRIL regions (yellow circles in Figure S3a). It seems that the dot-shaped voids gradually evolve into spindle-shaped voids of length of 28-90 μm in the No. 2 tomo-cell (yellow ellipses in Figure S3b). In the No. 3 tomo-cell, the spindle-shaped voids become dominant and they grow larger in size (Figure S3c). These spindle-shaped voids are also observable in the direction perpendicular to the Na/separator interface (Figure 1c2). This indicates that the spindle-shaped voids can grow in both the horizontal (along x-y plane) and vertical (along x-z plane) directions during electrochemical cycling. Figure S3d shows the generation of a large ruptured crack (roughly 376 μm long, 12.4-53.2 μm wide) through the NRIL region in the cycled No. 4 tomo-cell. Moreover, thin and slim cracks can be also found as highlighted by red arrows in Figure S3d. These slim cracks are very likely the unmatured ones and they are expected to grow during further electrochemical reactions. Looking at its electrochemical charge-discharge curve (Figure 1d1), one can clearly note a huge increase in overpotential upon cycling. This huge overpotential increase is caused very likely by these formed cracks that lead to a sluggish ion transport dynamic. The 3D volume renderings of the evolved Na anodes are shown in Figure 1a5-d5, which are in good agreement with the 2D image results.

For further quantitative analysis, the porosity of the formed NRIL after different cycling conditions is studied through data binarization and segmentation. The 3D rendering of the voids/cracks shown in Figure 2b1-b4, which are extracted from the segmented tomography data (Figure 2a1-a4), reveals graphically their evolution as a function of cycles. One can note obviously that the quantity of voids/cracks increase proportionally

with the increased capacity. Additional quantifications of the porosity and the surface area of the formed voids/cracks, which are shown in Figure 2c1,c2, demonstrate clearly that both values increase sharply during the stage II and they reach the maximum during the stage III. Together, these results reveal vividly the formation and three-stage evolution as well as its potential effects of NRIL in battery decay: 1) the initial formation of the dot-shaped voids (stage I); 2) the gradual growth of the dot-shaped voids into the spindle-shaped ones that are distributed randomly within the NRIL (stage II); 3) the further growth of the spindle-shaped voids into large ruptured cracks that could seriously block the transport channel of Na^+ ions (stage III).

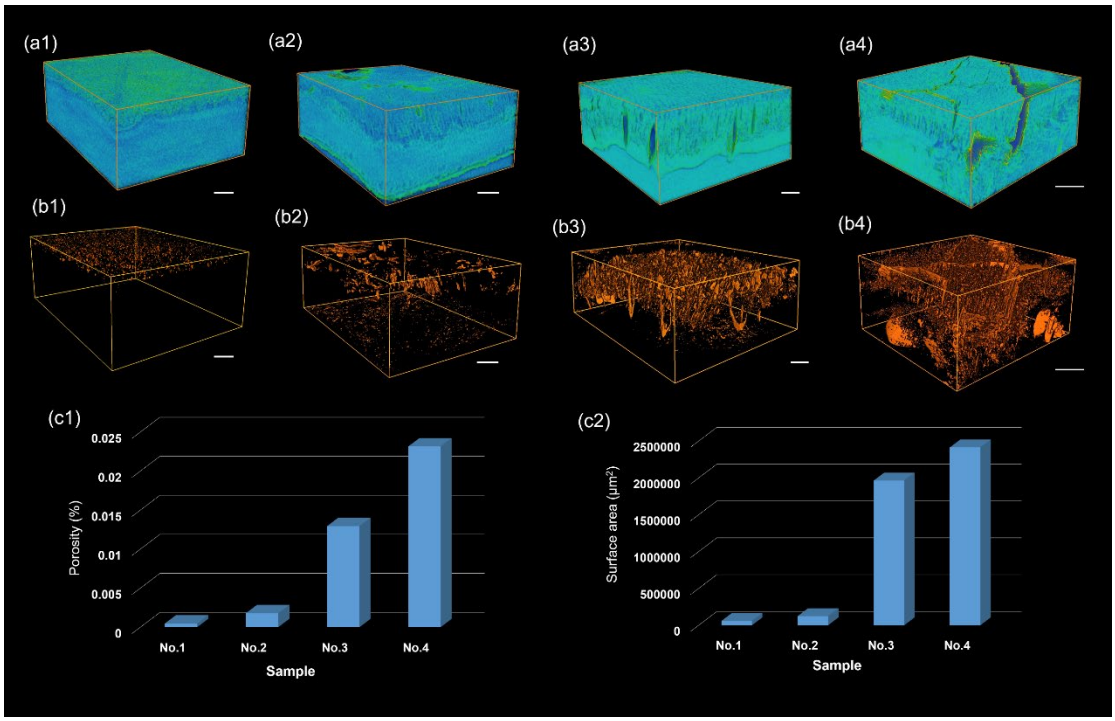

Figure 2. Reconstructed and segmented 3D volume of Na anodes after varied electrochemical conditions. (a1-a4) The 3D rendering of the Na anodes after electrochemical cycling. (b1-b4) The 3D view of the as-formed void/crack in the sodium reactive layer. (c1-c2) Quantification results of the volume and surface area of the formed voids. All scale bars are 100 μm.

2.2 *Morphology and components evolution of Na metal anode in NaOBs*

To further clarify the origins of the voids/cracks in Na metal anode detected by *in-situ* SXCT technique, Na anodes disassembled from Swagelok-cells after different electrochemical/chemical conditions are studied by postmortem scanning electron microscope (SEM). Specifically, a series of control experiments in which Na anodes

are subjected to four different handling conditions that aim to distinguish the individual influencing roles played by oxygen, electrolyte, and external current are conducted: resting the Na metal in pure oxygen atmosphere for 48 hrs (**Path 1**; influencing factor: oxygen); resting the Na metal in electrolyte with argon gas atmosphere for 48 hrs (**Path 2**; influencing factor: electrolyte); resting the Na metal in Swagelok-cell with an oxygen atmosphere for 48 hrs (**Path 3**; influencing factors: both oxygen and electrolyte); the Na metal as the anode cycling (0.1 mA cm^{-2} until cell failure) in Swagelok-cell with an oxygen atmosphere (**Path 4**; influencing factors: oxygen, electrolyte, and current). It is noted here that the Path 1-3 experiments are designed for identifying the formation prerequisites for the detected voids/cracks.

Figure S4 provide the SEM surface and cross-section results of the pristine Na metal and the treated Na metals (Path 1-4). And the interfacial layers formed under Path 1-4 are named by NRIL-n (n=1-4), respectively. One can note that the surface/cross-section of the pristine Na anode is relatively flat and smooth (Figure S4a-c). After processing by Path 1-4, the Na metal anodes display a much rougher and uneven surface morphology. After experiencing Path 1 and Path 2, one can note from their cross-sectional and zoom-in views that the NRIL thickness of the Na metal anode is respectively 25 μm (NRIL-1) and 46 μm (NRIL-2) (Figure S4d-i). After processing by Path 3 and Path 4, much thicker NRILs are visible in Figure S4j-o (NRIL-3: 354 μm; NRIL-4: 564 μm). Intriguingly, there are no detectable voids and cracks on NRIL-1,2 compared to NRIL-3,4. Therefore, these control experiments suggest that the excessive formation of the porous NRILs is greatly associated with the synergistic effects of O_2 and electrolyte (Path 3 and Path 4). Furthermore, one can discern a significant difference between porous NRIL-3 and NRIL-4. For the NRIL-3, the chemical parasitic reactions occur inside the cell, which form a porous interfacial layer on the surface of the bulk Na, indicating that the O_2-saturated electrolyte is more corrosive than the individual electrolyte. With the application of electrochemical conditions (Path 4), the porous NRIL-4, which traverses almost the entire thickness of the Na anode and covers both the top dense portion and the bottom porous portion is observed. It is speculated

that the formed dense portion at the upper edge of the porous NRIL is caused by a side effect exacerbated by electrochemical cycling. Additionally, large cracks shown in Figure S4o are generated at the tip of the voids in the porous layer of NRIL-4. These findings suggest that the external current during electrochemical cycling (Path 4) contributes significantly to the detected large voids/cracks.

Aiming to clarify the differences between the (electro)chemically developed NRILs, depth-profiling XPS and TOF-SIMS measurements are conducted, which can provide detailed surface and undersurface information about the composition of battery materials. The composition of the (electro)chemically formed NRILs determined by depth-profiling XPS are shown in Figure S5-S7 and Figure 3 respectively. Compared with the influence of separate oxygen (Path 1, Figure S5) or electrolyte (Path 2, Figure S6), the synergistic effect (Path 3, Figure S7) between them results in the production of more decomposition products (such as $ROCO_2Na$, CF_x, NaF, SO_3 and SO_2F *etc.*) on the Na surface. These results further prove that O_2 can facilitate electrolyte decomposition, resulting in the thickening and cracking of NRIL-3. To further clarify the compositional changes of the formed NRIL-4 during electrochemical cycling process, Na anodes disassembled from Swagelok-cells after different cycled total capacities (3.850 $mAhcm^{-2}$, 8.557 mAh cm^{-2} and 14.120 mAh cm^{-2}) are studied (Figure 3 and Figure 4). Regardless of the etching depth (0 s, 60 s, 120 s and 240 s), at larger cycling total capacity, the NRIL-4 contains more F, S content, and smaller O, C atomic ratios in the NaOBs (Figure 3a). Wherein, F, S containing species are primarily derived from the decomposition of $NaCF_3SO_3$ salts and meanwhile the diethylene glycol dimethyl ether (diglyme) solvents decompose to generate C, O containing organic compounds.

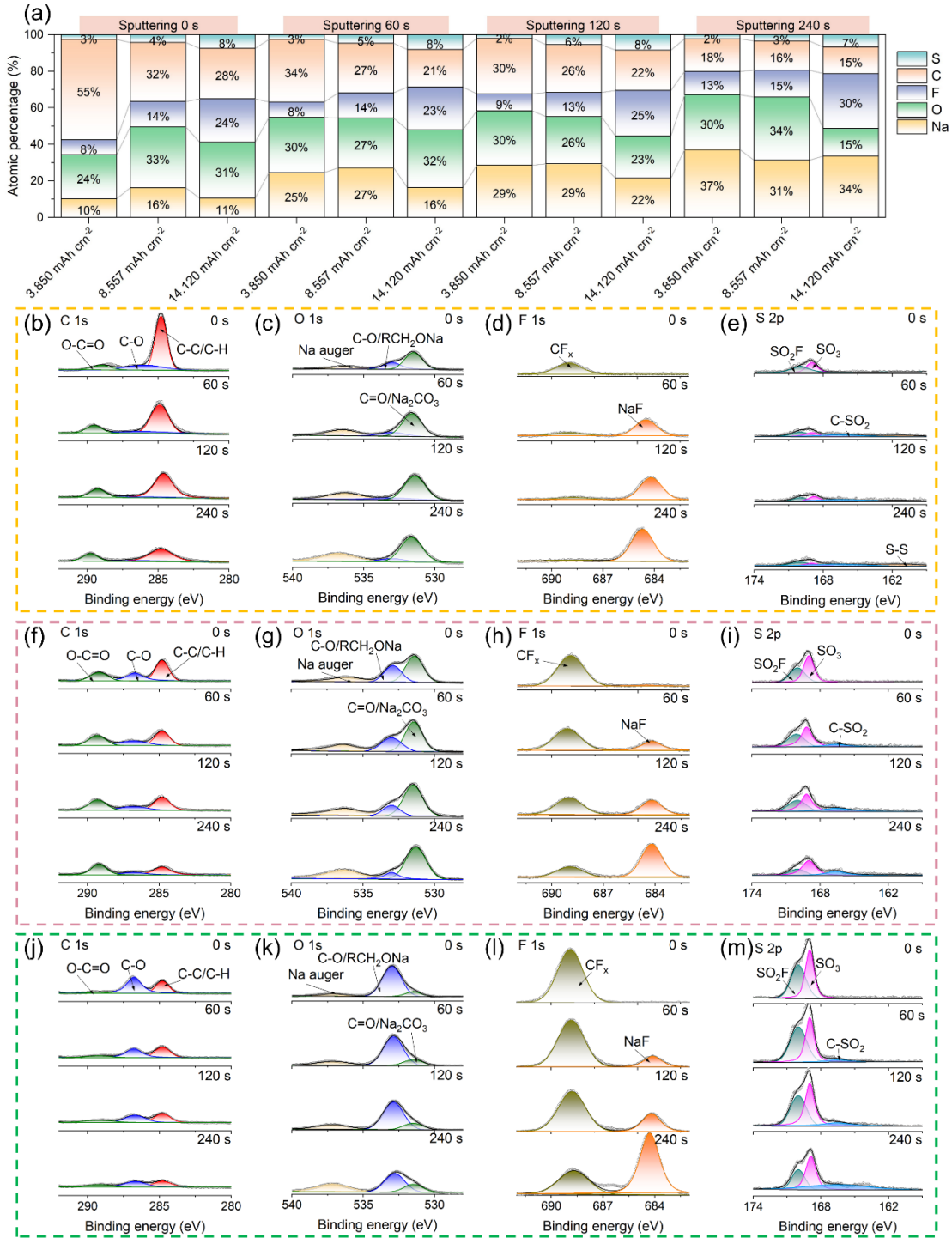

Figure 3. Postmortem compositional analysis of Na anodes by depth-profiling XPS. (a) The depth profile elemental distribution of the NRIL at three cycling capacities (3.850 mAhcm^{-2}, 8.557 mAh cm^{-2} and 14.120 mAh cm^{-2}). C 1s, O 1s, S 2p, and F 1s depth-profiling XPS spectra of processed Na anode at 3.850 mAh cm^{-2} (b-e), 8.557 mAh cm^{-2} (f-i) and 14.120 mAh cm^{-2} (j-m) cycling capacity. Sputtering times are 0, 60, 120, and 240 s.

Specifically, the O 1s, C 1s, F 1s and S 2p depth-profiling XPS spectrums of the Na anodes in NaOBs cycled after different total capacities are also provided (Figure 3b-m).

In the C 1s spectrum, the peak at 284.8 eV, corresponding to C-C/C-H bonds, representing C-containing organic compounds, progressively diminishes as the NaOBs cycle capacity increases (Figure 3b,f,g). Notably, as the cycle prolongs (small to large cycled capacity), the 531 eV peak (O 1s spectrum) gradually decreases while the 533 eV peak (O 1s spectrum) gradually increases (Figure 3c,g,k). The decrease of 531 eV peak may be due to the accumulation of by-products in NRIL masking the Na_2CO_3 on the original Na metal surface. Meanwhile, the severe reaction between diglyme solvents and Na metal anode will lead to the substantial production of RCH_2ONa within the NRIL, resulting in increase of 533 eV peak [28,53]. More importantly, the content of species containing F (Figure 3d,h,l) and S (Figure 3e,i,m), such as CF_x (688.5 eV in F 1s spectrum), NaF (684 eV in F 1s spectrum), SO_2F (170 eV in S 2p spectrum) and SO_3 (168.8 eV in S 2p spectrum), undergoes a sharp increase by around three times upon cycling (Figure 3a). These findings provide evidence that the severe side reactions between the Na anode and electrolyte play a huge role in the thickening and cracking of the NRIL-4 during cycling. The reaction between $NaCF_3SO_3$ and Na anode is more intense than that of diglyme solvents.

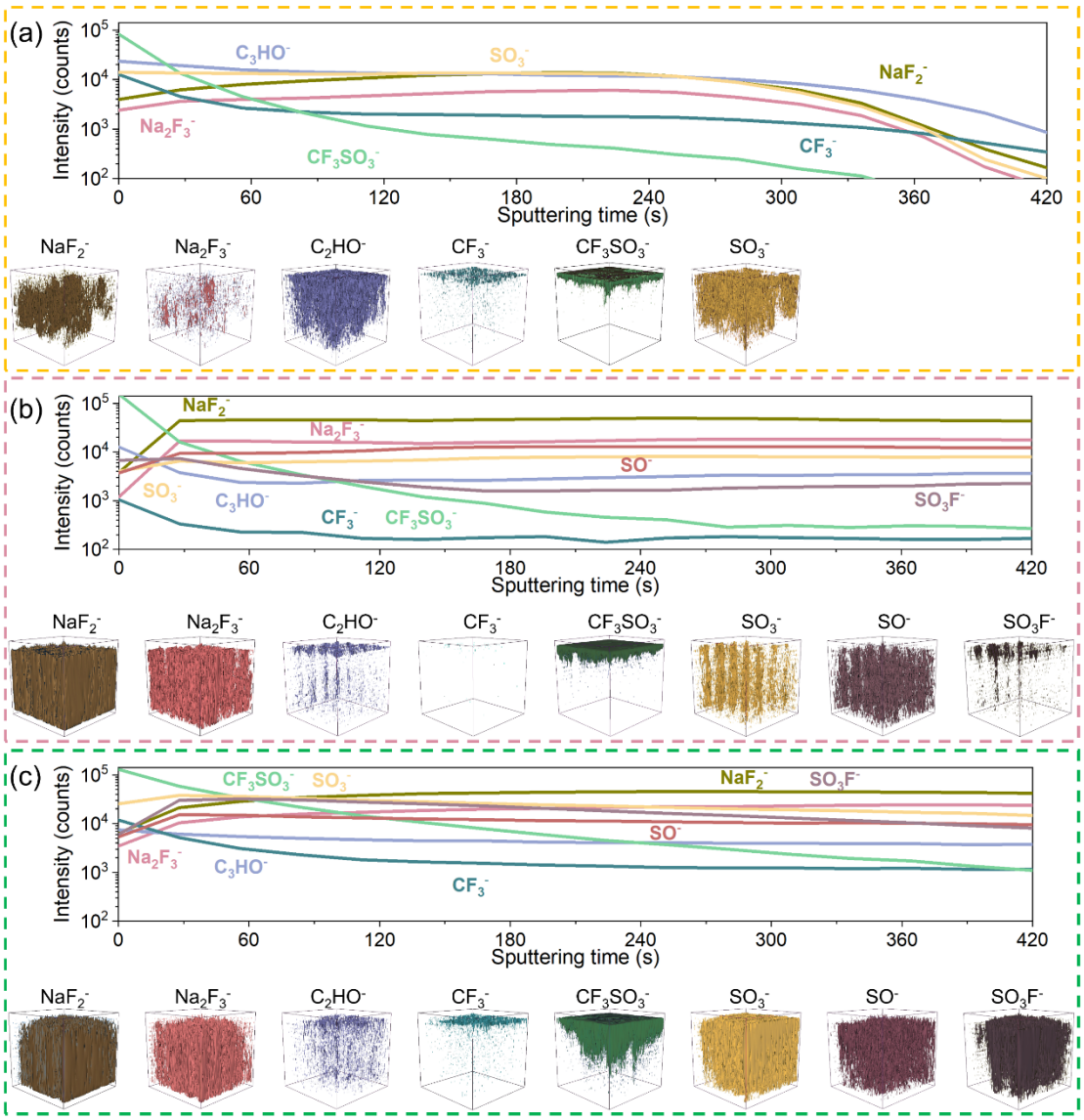

Figure 4. TOF-SIMS 3D reconstruction with corresponding depth profiles of Na anodes. The Na anodes were disassembled from Swagelok-cells after cycling at 3.850 mAh cm^{-2} (a), 8.557 mAh cm^{-2} (b) and 14.120 mAh cm^{-2} (c) cycling capacity.

Subsequently, TOF-SIMS measurement is performed to in-depth analyze the compositions of the deeper regions (etching depth: 420 s) of the NRIL-4 within the NaOBs cycled for 3.850 mAh cm^{-2}, 8.557 mAh cm^{-2} and 14.120 mAh cm^{-2}, respectively (Figure 4). At a cycling total capacity of 3.850 mAh cm^{-2}, both the $NaCF_3SO_3$ salt and diglyme solvent undergo initial decomposition on the Na anode, resulting in the formation of NRIL-4. After a 300s duration etching (Figure 4a), side reaction product concentrations have significantly decreased. With continued cycling, the Na anode surface accumulates much more F and S-containing species (NaF_2^-, $Na_2F_3^-$, CF_3^-,

$CF_3SO_3^-$, SO_3^-, SO^-, SO_3F^-) as depicted in Figure 4b,c. When the cycling total capacity is 8.557 mAh cm^{-2}, the content of F and S-containing species significantly surpasses that of C_2HO^- (Figure 4c). This result further proves that the reaction between $NaCF_3SO_3$ and Na anode is more intense than that of diglyme solvents. Hence, for NaOBs, it is crucial to use a Na salt with superior electrochemical stability. Additionally, one can note that all the by-products (C_2HO^-, NaF_2^-, $Na_2F_3^-$, CF_3^-, $CF_3SO_3^-$, SO_3^-, SO^-, SO_3F^-) exhibit non-uniform distribution within the NRIL, which can result in an uneven stress distribution, ultimately leading to crack formation (Figure 4c).

In summary, during the resting process electrolyte (both solvent and salt) will inevitably react with Na metal. Upon electrochemical cycling, oxygen will promote the reaction between electrolyte and Na metal to form NRIL-4. During this period, the prevailing parasitic reaction dominated by $NaCF_3SO_3$ salt leads to the generation of unevenly distributed by-products within the NRIL-4. The continuous thickening and cracking of the NRIL-4 may lead to severe decay in NaOBs, including low Coulombic efficiency, a sharp increase in polarization potential, and poor cycling performance (Figure 1d1). Furthermore, these unevenly distributed by-products within the NRIL-4, which possess varied mechanical properties, would facilitate NRIL-4 cracking and accelerate the mechanical degradation of Na anodes, as further discussed in the next section.

2.3 *Discussion of the evolving voids/cracks from the corrosion science viewpoint and a relevant FEA simulation*

The postmortem studies demonstrate that the porous NRIL could evolve under merely chemical-resting condition of **Path 3** (Figure S4k-l), the process of which will exacerbate under electrochemical conditions of **Path 4** (Figure S4n-o and Figure 1a5-d5). From the perspective of corrosion science, it appears that pitting corrosion and stress corrosion cracking are the two dominant corrosion types responsible for the observed changes of Na anodes.[54] The pitting corrosion is a unique type of anodic

dissolution of metal and its major occurrence condition is an electrochemical potential shift in the direction of a more positive one than a certain critical value, considered as pitting potential. During the chemical resting (**Path 3**), it is very likely that pitting occurs due to the existence of the corrosive electrolyte that contains strongly oxidizing oxygen. This process would be accelerated during cycling (**Path 4**) by the externally applied electrochemical potential, which shifts the electrochemical potential to a higher one and drives rapid Na electrodissolution. Hence, dot-shaped voids are generated after pitting corrosion. Meanwhile, these dot-shaped voids can serve as concentrators of stress where cracks could be formed.[55] The stress corrosion cracking requires the simultaneous presence of corrosive medium and mechanical stress.[56] Previous studies in stress corrosion cracking suggest that when the corrosive medium reaches the bottom of the crack, it causes new centers of stress concentrator from which new cracks are afterwards evolved.[56] The underlying reason is due to the fact that the corrosion reactions that builds up constantly stress concentrations at the crack tip. This stress corrosion cracking during **Path 3** can be also aggravated during **Path 4** because the externally applied electromotive force could enhance the corrosion reactions on the one hand, and on the other hand facilitate the stress generation by promoting the irreversible transformation of Na to porous NRIL. In the meantime, the unevenly distributed by-products within the NRIL such as the F, S, C, O containing species revealed by the depth-profiling XPS and TOF-SIMS measurements in section 2.2, would also contribute significantly to both the stress buildup and crack formation due to their different and varying mechanical properties, e.g., the Young's modulus, the fracture toughness, the volumetric strain, etc.[57-58] The formed crack morphology depends on various aspects and the currently observed spindle-shaped crack may be resulted from the unique metallurgical factors of Na and specific environmental factors of electrolyte.[59-60]

The above analysis highlights the complexity and interdependence of electrochemical, chemical, and mechanical coupling during the dynamic evolution of voids/cracks in NRIL-4 accompanying electrochemical cycling. However, the fundamental electro-

chemo-mechanical coupling during Na electrodissolution and deposition remains elusive. To clarify this, FEA method is employed due to its versatile capability to model the interfacial evolution of alkali metal/electrolyte and the electrode reactions.[61-62] During the current simulation, a coupled diffusion-deformation model that involves the concentration changes of Na^+ ion in NRIL-4 as well as the spatial distribution of stress in the spindle-shaped voids is created and used. A full illustration of the simulation is shown in Figure S9 and the simulation results during electrochemical dissolution/deposition are displayed in Figure 5. (Note that the electrode surrounding the voids in this model is treated as porous and filled with electrolyte and only the changes of the voids in the longitudinal direction are modeled. For simplicity, the effects of the by-products are not simulated)

Figure 5a-f show the simulation results during Na electrodissolution and Figure 5g-i show those during Na electrodeposition. Figure 5a,d show two snapshots of the spindle-shaped voids after Na electrodissolution for respectively 20 min and 70 min. These two figures clearly demonstrate the heterogeneous Na^+ ion distribution around the spindle-shape void (the black outline), that is, an obvious increase in Na^+ ion concentration within the void caused from the continuous Na electrodissolution. The corresponding contour plots of the induced von Mises stress distribution are shown in Figure 5b,e and the zoom-in views in Figure 5c,f. These results suggest that the maximum stress is concentrated at the tapered end of the spindle-shaped void where further crack growth is very likely to initiate. This simulation result resembles the scenario occurred during stress corrosion cracking. From the simulation results after Na electrodeposition for 30 min (Figure 5g, t=100 min for the whole simulation), one can observe an obvious Na^+ ion concentration gradient across the spindle-shape void. The unbalanced concentration gradient at the inner and the outer void may be triggered by a heterogenous Na electrodeposition, which would also lead to an uneven spatial distribution of mechanical stress. This is confirmed by the corresponding von Mises stress simulation results (Figure 5h,i) and the results also show that the maximum stress is concentrated at the tapered end of the spindle-shaped void, as well. These von Mises stress simulation

results demonstrate that the maximum stress is concentrated at the tip end of the spindle-shaped void and this concentrated stress, once reaches values larger than the critical fracture stress (or the stress corrosion threshold from the stress corrosion perspective) of Na, may eventually drive the continuous crack extension during the repeated Na electrodissolution/deposition.[63] This simulated crack propagation behavior bears some similarities to the Mode I fracture scenario[64] (which describes the extension of initial surface cracks by the focusing of the ionic current in beta alumina electrolyte) in fracture mechanics and it also mirrors the role of mechanical stress during the stress corrosion cracking. Aiming to further reveal the fundamental correlation between the mechanical stress and the electrochemical process at the tip end of the spindle-shape voids, the evolution of the Na^+ ion concentration and the Von Mises stress are analyzed and the results are shown in Figure 5j,k. From these two figures, one can clearly observe that the Von Mises stress peaks at 70 min, coinciding with the maximum Na^+ ion concentration. This result suggests that the local electrochemical process occurring at the crack tip could build up stress concentration, which in turn is responsible for further crack propagation.

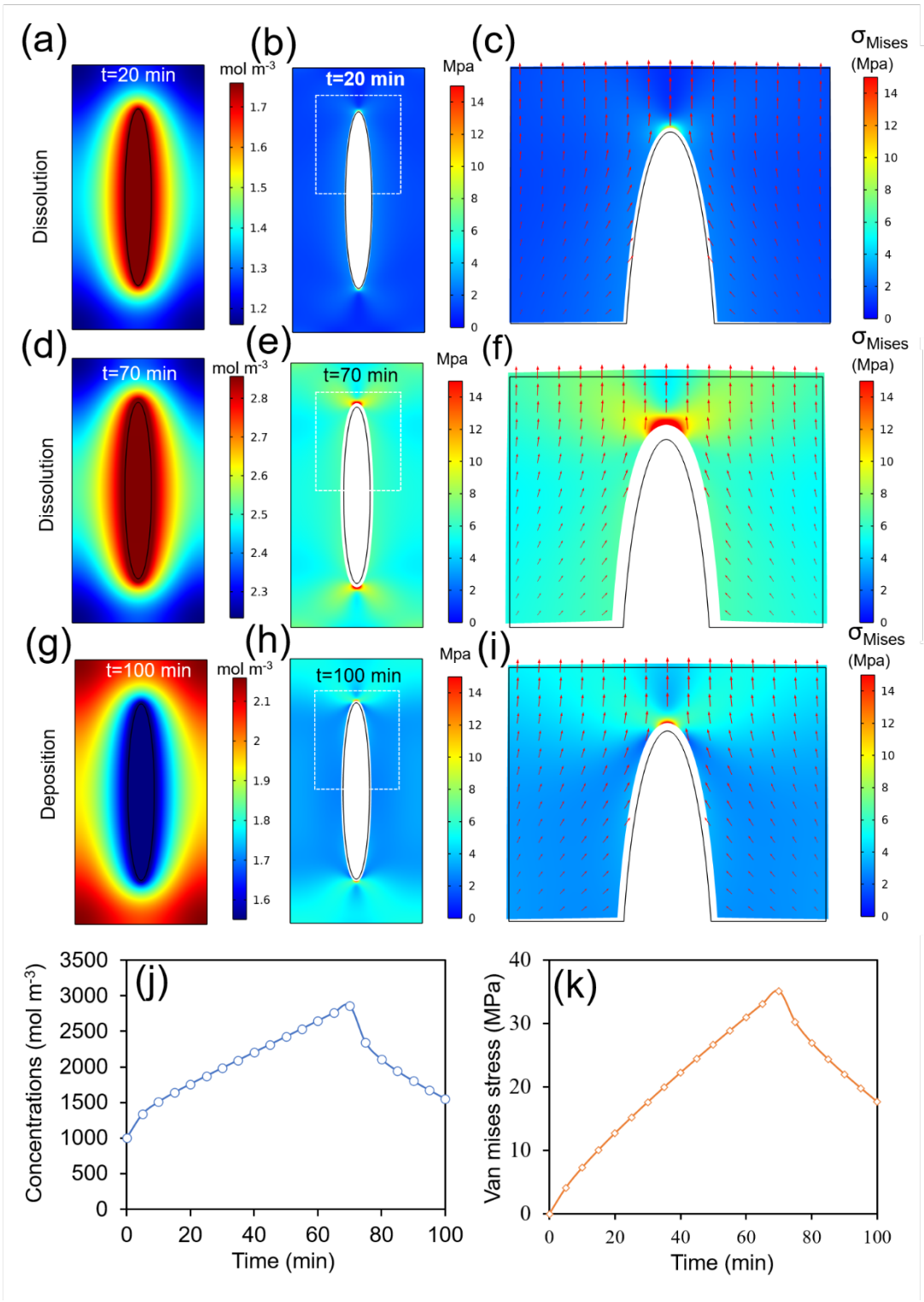

Figure 5. Finite element modeling of the electro-chemo-mechanical coupling at Na anode during electrodissolution and deposition. The Na^+ ion concentration distribution around a spindle-shaped void region after electrodissolution for 20 min (a), 70 min (d) and after electrodeposition for 30 min (g), respectively. The von Mises stress distribution around the spindle-shaped void after electrodissolution for 20 min (b), 70 min (e) and after deposition for 30 min (h), respectively. (c, f, i) The corresponding zoom-in views of the von Mises stress distribution at the tip of spindle-shaped void. (j) The Na^+ ion concentration changes at the tip of the spindle-shaped void during simulation.

(k) The Von Mises stress change at the tip of the spindle-shaped void during simulation.

2.4 Summary of the Na anode degradation evolution and a further discussion of the NRIL

On the basis of the experimental characterizations and the simulation results, the proposed evolution of Na anodes during electrochemical cycling is schematically exhibited in Figure 6. Compared with the pristine state of Na anode (Figure 6a), a number of dot-shaped voids, as schematically shown in Figure 6b, appear when the Na electrodissolution from the NRIL region is faster than that it could be replenished (e.g., self-diffusion).[65-66] Once the voids/cracks are generated the electrolyte will very likely flow into them, leading to an inhomogeneous distribution of Na^+ ion flux that influence subsequent electrodeposition and dissolution.[63] Meanwhile, from the corrosion science point of view, the freshly exposed Na metal in the void/crack region may continuously react with the O_2-saturated electrolyte, which is strongly oxidative. The volumetric changes accompanying these side-reactions serve as the mechanical stress that induces stress corrosion cracking, which is exacerbated under electrochemical condition. In turn, these generated by-products, together with the formed voids/cracks, would significantly deteriorate the structural integrity of Na anode as well as the ionic transportation. This may also lead to the (electro)chemical deactivation of the NRIL, to some extent, according to previous reports.[67] During the subsequent stripping process, part of the Na^+ ion would be supplied from the electrodissolution of Na around the void/crack region, resulting in a continuous growth of the initially formed voids/cracks (Figure 6c). In addition, fresh Na bulk will be also electrodissolved due to the deactivation of the NRIL, leading to the accumulation of voids/cracks and the inward growth of the NRIL towards the Na bulk metal (Figure 6d).

It has to be noted that during the aforementioned evolution of Na anode, besides the volumetric-change induced mechanical stress that facilitates the stress corrosion cracking, repeated Na electrodeposition and dissolution around the spindle-like voids would also produce concentrated stresses. This concentrated stress, together with the former type, could further drive void propagation and eventually lead to the formation

of ruptured cracks within the NRIL when its value is larger than the critical fracture stress (or the stress corrosion threshold for stress corrosion cracking) of Na.[68-70] Taken together, it appears that mechanical stress caused crack propagation and the inward-growing NRIL could lead inevitably to a sluggish ion transportation and an increased overpotential, ultimately causing an irreversible mechanical failure of Na anode and the NaOBs performance degradation.

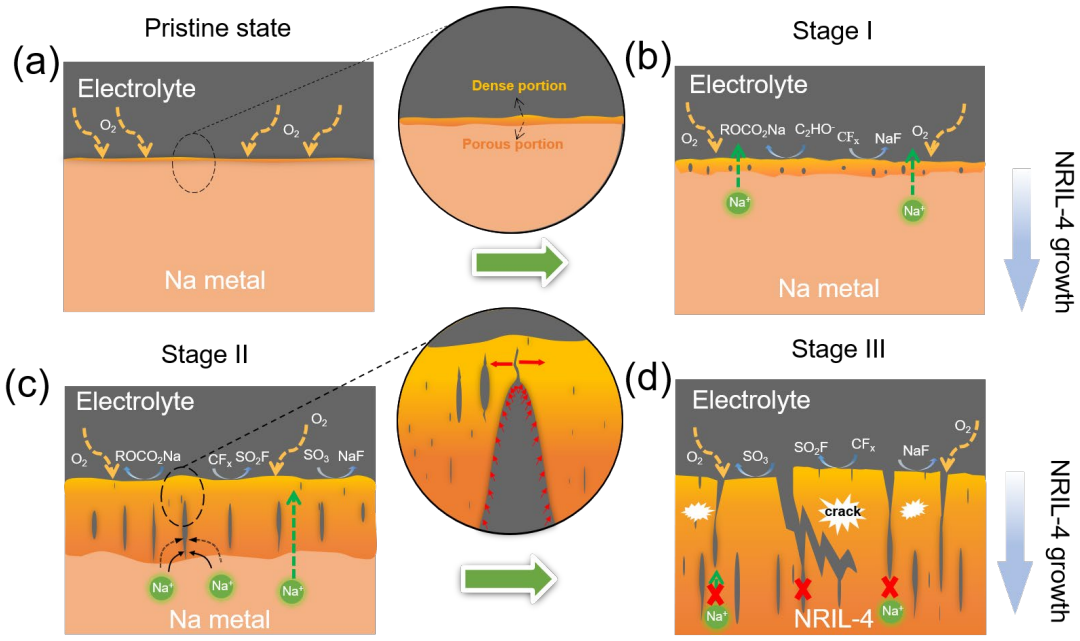

Figure 6. A schematic illustration of the morphological evolution of Na anodes under different electrochemical conditions. (a) Pristine Na anode without electrochemical cycling. (b) The formation of NRIL with dot-shaped voids in Stage I. (c) The continuing growth of the dotted voids into spindle-shaped voids in stage II, and the inwardly growing NRIL to the Na bulk. (d) The mechanical failure of Na metal anodes caused from the continuous growth of the spindle-shaped voids.

The reported dynamic evolution of Na anode and the porous NRIL under (electro)chemical conditions are essential in developing NaOBs built with (electro)chemically stable Na metal anode. From the corrosion science point of view, the current work suggests that the growth of NRIL initiates already in the O_2-saturated electrolyte after the NaOBs are assembled. And this process is enhanced under electrochemical cycling condition. For this reason, it suggests that the protection of the Na metal anode is an important consideration that should be taken into account when

building the NaOBs. For this point, some available strategies such as employing chemically stable electrolyte [71-73] and adopting protective layers on Na metal[74-76] may help to mitigate the formation of NRIL. In addition, considering that the externally applied electromotive force during cycling could exacerbate the unwanted reactions between Na anode and the electrolyte, this implies that developing Na salt and electrolytes that possess a sufficient electrochemical stability window is highly desirable.[75] From the mechanical point of view, the role of the mechanical stress during crack propagation indicates that developing Na anodes with high mechanical strength is critical to prevent their mechanical fracture failure during long-term NaOBs cycling. In this respect, constructing carbon or other metal skeleton enforced Na anodes seems to be a plausible way to enhance their overall mechanical strength and minimize the localized stress concentration that causes their mechanical failure. Last but not the least, bearing in mind that the NaOBs involve a highly oxidative environment that could severely aggravate Na anode degradation, the current research suggests that merely utilizing a single strategy may not be sufficient to resolve the existing challenges. Therefore, synchronizing multi-strategy approaches of specific goals may render the Na anode possible for building performance improved NaOBs.

In summary, this investigation unravels the mechanical degradation of NaOBs via non-destructive 3D synchrotron X-ray tomography technique. This technique reveals the dynamic evolution of Na anode and the gradual formation of a Na reactive interphase layer (NRIL) in NaOBs during battery operation. Together with the gradually degraded battery performance, these results suggest a detrimental effect of the electrochemically formed NRIL. Depth-profiling XPS and TOF-SIMS characterizations are conducted to provide the detailed structure and composition information of the NRIL. It is found that O_2 contributes significantly to the decomposition of the electrolyte, which is dominated by the decomposition of $NaCF_3SO_3$ salts, leading to thickening and cracking of the NRIL. On the basis of these experimental findings, the formation and growth of the voids in the NRIL are suggested to undergo three stages, i.e., the dot-shaped voids (stage I) growing into the spindle-

shaped voids (stage II) and eventually into ruptured cracks (stage III). Control studies demonstrate that the porous NRIL could evolve under purely chemical-resting conditions and its formation process would accelerate under electrochemical cycling conditions. Corrosion science (pitting corrosion and stress corrosion cracking) and fracture mechanics are adopted to interpret its evolution. FEA simulations are conducted to understand this evolution further and the results suggest that the mechanical stress concentrated at the tip of the spindle-like voids drives their further propagation. Overall, this work provides mechanistic insights into the failure mechanism of Na anodes in NaOBs during electrochemical cycling and the improved understanding of the evolution of metallic Na anodes may hopefully trigger further development of engineering strategies to suppress the Na anode fracture failure to advance the development of NaOBs for practical applications.

Acknowledgements

This work is sponsored by the National Natural Science Foundation of China (52101276, 22102206), and Taishan Scholars of Shandong Province (ts201511063). The authors acknowledge DESY (Hamburg, Germany), a member of the Helmholtz Association HGF, for the provision of the P05 beamline experimental facility for conducting the synchrotron X-ray tomography measurements. The authors also acknowledge the Helmholtz-Zentrum Berlin für Materialien und Energie for the allocation of synchrotron radiation beam time.

Author contributions

Xia Zhang and Shenghang Zhang contributed equally to this work. Xia Zhang, Jie Lu, Fengcheng Tang, Fu Sun, and Kang Dong assembled and tested the cells. Fu Sun, Henning Markötter and Ingo Manke designed the cell. André Hilger, Markus Osenberg, Henning Markötter and Fabian Wilde aided in synchrotron characterizations. André Hilger, Ingo Manke, Zhenjiang Yu and Fu Sun aided in analyzing the synchrotron data sets. Xia Zhang, Jie Lu, Shenghang Zhang, Gaojie Xu conducted and analyzed the XPS and TOF-SIMS measurements. Xia Zhang, Zhenjiang Yu, Shu Zhang, Gaojie Xu and Jingwen Zhao composed the manuscript. Fu Sun, Gaojie Xu, Jingwen Zhao and Guanglei Cui revised the manuscript. All authors contributed to the data interpretation and the discussion of the results.

Corresponding authors

Fu Sun: sunfu@qibebt.ac.cn

Guanglei Cui: cuigl@qibebt.ac.cn

Competing of Interest

The authors declare no conflict of interest.

Data Availability Statement

The data that support the findings of this study are available in the supplementary material of this article.

Supporting Information

Supporting Information is available from the Wiley Online Library or from the author. The supporting information contains the experimental details, additional data and FEA computational method details.

Reference

[1] S. Dong, S. Yang, Y. Chen, C. Kuss, G. Cui, L. R. Johnson, X. Gao, P. G. Bruce, *Joule* **2022**, *6*, 185.

[2] P. Hartmann, C. L. Bender, M. Vračar, A. K. Dürr, A. Garsuch, J. Janek, P. Adelhelm, *Nat. Mater.* **2013**, *12*, 228.

[3] G. Leverick, G. Alvarez Perez, R. M. Stephens, Y. Shao-Horn, *ACS Energy Lett.* **2023**, *8*, 1584.

[4] K. K. Velinkar, A. V. Gunten, J. Greeley, E. Nikolla, *ACS Energy Lett.* **2023**, *8*, 4555.

[5] P. Chen, Y. Li, X. Cheng, H. Yu, X. Yin, Y. Jiang, H. Zhang, S. Li, F. Huang, *J. Power Sources* **2023**, *574*, 233164.

[6] H. Yu, D. Jiang, X. Cheng, P. Lu, S. Li, H. Zhang, Y. Jiang, F. Huang, *Adv. Funct. Mater.* **2023**, *33*, 2307628.

[7] S. Han, C. Cai, F. Yang, Y. Zhu, Q. Sun, Y. G. Zhu, H. Li, H. Wang, Y. Shao-Horn, X. Sun, M. Gu, *ACS Nano* **2020**, *14*, 3669.

[8] X. Kong, P. E. Rudnicki, S. Choudhury, Z. Bao, J. Qin, *Adv. Funct. Mater.* **2020**, *30*, 1910138.

[9] J. Wang, Y. Ni, J. Liu, Y. Lu, K. Zhang, Z. Niu, J. Chen, *ACS Cent. Sci.* **2020**, *6*, 1955.

[10] J. Pan, Y. Zhang, F. Sun, M. Osenberg, A. Hilger, I. Manke, R. Cao, S. X. Dou, H. J. Fan, *Angew. Chem. Int. Ed.* **2023**, *62*, e202219000.

[11] J. L. Gómez-Cámer, I. Ruiz de Larramendi, M. Enterría, I. Lozano, B. Acebedo, D. Bordeau, N. Ortiz-Vitoriano, *J. Mater. Chem. A* **2022**, *10*, 2398.

[12] X. He, Y. Ni, Y. Li, H. Sun, Y. Lu, H. Li, Z. Yan, K. Zhang, J. Chen, *Adv. Mater.* **2022**, *34*, 2106565.

[13] C. Zhou, K. Lu, S. Zhou, Y. Liu, W. Fang, Y. Hou, J. Ye, L. Fu, Y. Chen, L. Liu, Y. Wu, *Chem. Commun.* **2022**, *58*, 8014.

[14] Y. G. Zhu, G. Leverick, A. Accogli, K. Gordiz, Y. Zhang, Y. Shao-Horn, *Energy Environ. Sci.* **2022**, *15*, 4636.

[15] P. Mao, H. Arandiyan, S. S. Mofarah, P. Koshy, C. Pozo-Gonzalo, R. Zheng, Z. Wang, Y. Wang, S. K. Bhargava, H. Sun, Z. Shao, Y. Liu, *Energy Adv.* **2023**, *2*, 465.

[16] K. Song, D. A. Agyeman, M. Park, J. Yang, Y.-M. Kang, *Adv. Mater.* **2017**, *29*, 1606572.

[17] C. Gong, S. D. Pu, S. Zhang, Y. Yuan, Z. Ning, S. Yang, X. Gao, C. Chau, Z. Li, J. Liu, L. Pi, B. Liu, I. Capone, B. Hu, D. L. R. Melvin, M. Pasta, P. G. Bruce, A. W. Robertson, *Energy Environ. Sci.* **2023**, *16*, 535.
[18] L. Gao, J. Chen, Q. Chen, X. Kong, *Sci. Adv.* **2022**, *8*, eabm4606.
[19] X. Lin, Q. Sun, K. Doyle Davis, R. Li, X. Sun, *Carbon Energy* **2019**, *1*, 141.
[20] S. Zhao, L. Li, F. Li, S.-L. Chou, *Electrochem. Commun.* **2020**, *118*, 106797.
[21] A. Von Gunten, K. Velinkar, E. Nikolla, J. Greeley, *Chem. Mater.* **2023**, *35*, 5945.
[22] T. Liu, G. Kim, M. T. L. Casford, C. P. Grey, *J. Phys. Chem. Lett.* **2016**, *7*, 4841.
[23] N. Ortiz-Vitoriano, I. Monterrubio, L. Garcia-Quintana, J. M. López del Amo, F. Chen, T. Rojo, P. C. Howlett, M. Forsyth, C. Pozo-Gonzalo, *ACS Energy Lett.* **2020**, *5*, 903.
[24] X. Lin, Y. Sun, Q. Sun, J. Luo, Y. Zhao, C. Zhao, X. Yang, C. Wang, H. Huo, R. Li, X. Sun, *Adv. Energy Mater.* **2021**, *11*, 2003789.
[25] H. Yadegari, X. Sun, *Trends Chem.* **2020**, *2*, 241.
[26] H. Liu, M. Osenberg, L. Ni, A. Hilger, L. Chen, D. Zhou, K. Dong, T. Arlt, X. Yao, X. Wang, I. Manke, F. Sun, *J. Energy Chem.* **2021**, *61*, 61.
[27] S. Wu, Y. Qiao, K. Jiang, Y. He, S. Guo, H. Zhou, *Adv. Funct. Mater.* **2018**, *28*, 1706374.
[28] N. Zhao, C. Li, X. Guo, *Phys. Chem. Chem. Phys.* **2014**, *16*, 15646.
[29] R. S. Assary, J. Lu, P. Du, X. Luo , X. Zhang, Y. Ren, L. A. Curtiss, K. Amine, *ChemSusChem* **2013**, *6*, 51.
[30] C. L. Bender, B. Jache, P. Adelhelm, J. Janek, *J. Mater. Chem. A* **2015**, *3*, 20633.
[31] M. Marinaro, P. Balasubramanian, E. Gucciardi, S. Theil, L. Jörissen, M. Wohlfahrt-Mehrens, *ChemSusChem* **2015**, *8*, 3139.
[32] S. Zhao, B. Qin, K.-Y. Chan, C.-Y. V. Li, F. Li, *Batteries Supercaps* **2019**, *2*, 725.
[33] X.-M. Lin, X.-T. Yang, H.-N. Chen, Y.-L. Deng, W.-H. Chen, J.-C. Dong, Y.-M. Wei, J.-F. Li, *J. Energy Chem.* **2023**, *76*, 146.
[34] Y. Xiang, G. Zheng, Z. Liang, Y. Jin, X. Liu, S. Chen, K. Zhou, J. Zhu, M. Lin, H. He, J. Wan, S. Yu, G. Zhong, R. Fu, Y. Li, Y. Yang, *Nat. Nanotechnol.* **2020**, *15*, 883.
[35] F. Sun, X. He, X. Jiang, M. Osenberg, J. Li, D. Zhou, K. Dong, A. Hilger, X. Zhu, R. Gao, X. Liu, K. Huang, D. Ning, H. Markötter, L. Zhang, F. Wilde, Y. Cao, M. Winter, I. Manke, *Mater. Today* **2019**, *27*, 21.
[36] F. Tang, Z. Wu, C. Yang, M. Osenberg, A. Hilger, K. Dong, H. Markötter, I. Manke, F. Sun, L. Chen, G. Cui, *Small Methods* **2021**, *5*, 2100557.
[37] B. Lee, E. Paek, D. Mitlin, S. W. Lee, *Chem. Rev.* **2019**, *119*, 5416.
[38] J. Kasemchainan, S. Zekoll, D. Spencer Jolly, Z. Ning, G. O. Hartley, J. Marrow, P. G. Bruce, *Nat. Mater.* **2019**, *18*, 1105.
[39] J. A. Lewis, S. E. Sandoval, Y. Liu, D. L. Nelson, S. G. Yoon, R. Wang, Y. Zhao, M. Tian, P. Shevchenko, E. Martínez-Pañeda, M. T. McDowell, *Adv. Energy Mater.* **2023**, *13*, 2204186.
[40] J. Scharf, M. Chouchane, D. P. Finegan, B. Lu, C. Redquest, M.-c. Kim, W. Yao, A. A. Franco, D. Gostovic, Z. Liu, M. Riccio, F. Zelenka, J.-M. Doux, Y. S. Meng, *Nat. Nanotechnol.* **2022**, *17*, 446.
[41] F. Sun, C. Wang, M. Osenberg, K. Dong, S. Zhang, C. Yang, Y. Wang, A. Hilger, J. Zhang, S. Dong, H. Markötter, I. Manke, G. Cui, *Adv. Energy Mater.* **2022**, *12*, 2103714.
[42] Z. Yu, R. Li, K. Cai, Y. Yao, J. Deng, S. Lou, M. Lu, Q. Pan, G. Yin, Z. Jiang, J. Wang, *J.*

Energy Chem. **2021**, *58*, 355.
[43] Z. Zhang, K. Dong, K. A. Mazzio, A. Hilger, H. Markötter, F. Wilde, T. Heinemann, I. Manke, P. Adelhelm, *Adv. Energy Mater.* **2023**, *13*, 2203143.
[44] C. Zhu, T. Fuchs, S. A. L. Weber, F. H. Richter, G. Glasser, F. Weber, H.-J. Butt, J. Janek, R. Berger, *Nat. Commun.* **2023**, *14*, 1300.
[45] R. F. Ziesche, T. M. M. Heenan, P. Kumari, J. Williams, W. Li, M. E. Curd, T. L. Burnett, I. Robinson, D. J. L. Brett, M. J. Ehrhardt, P. D. Quinn, L. B. Mehdi, P. J. Withers, M. M. Britton, N. D. Browning, P. R. Shearing, *Adv. Energy Mater.* **2023**, *13*, 2300103.
[46] J. A. Lewis, F. J. Q. Cortes, Y. Liu, J. C. Miers, A. Verma, B. S. Vishnugopi, J. Tippens, D. Prakash, T. S. Marchese, S. Y. Han, C. Lee, P. P. Shetty, H.-W. Lee, P. Shevchenko, F. De Carlo, C. Saldana, P. P. Mukherjee, M. T. McDowell, *Nat. Mater.* **2021**, *20*, 503.
[47] Z. Ning, G. Li, D. L. R. Melvin, Y. Chen, J. Bu, D. Spencer-Jolly, J. Liu, B. Hu, X. Gao, J. Perera, C. Gong, S. D. Pu, S. Zhang, B. Liu, G. O. Hartley, A. J. Bodey, R. I. Todd, P. S. Grant, D. E. J. Armstrong, T. J. Marrow, C. W. Monroe, P. G. Bruce, *Nature* **2023**, *618*, 287.
[48] Z. Su, E. Decencière, T.-T. Nguyen, K. El-Amiry, V. De Andrade, A. A. Franco, A. Demortière, *NPJ Comput. Mater.* **2022**, *8*, 30.
[49] Z. Ning, D. S. Jolly, G. Li, R. De Meyere, S. D. Pu, Y. Chen, J. Kasemchainan, J. Ihli, C. Gong, B. Liu, D. L. R. Melvin, A. Bonnin, O. Magdysyuk, P. Adamson, G. O. Hartley, C. W. Monroe, T. J. Marrow, P. G. Bruce, *Nat. Mater.* **2021**, *20*, 1121.
[50] F. Sun, M. Osenberg, K. Dong, D. Zhou, A. Hilger, C. J. Jafta, S. Risse, Y. Lu, H. Markötter, I. Manke, *ACS Energy Lett.* **2018**, *3*, 356.
[51] L. Eifert, N. Bevilacqua, K. Köble, K. Fahy, L. Xiao, M. Li, K. Duan, A. Bazylak, P.-C. Sui, R. Zeis, *ChemSusChem* **2020**, *13*, 3154.
[52] S. Hao, J. J. Bailey, F. Iacoviello, J. Bu, P. S. Grant, D. J. L. Brett, P. R. Shearing, *Adv. Funct. Mater.* **2021**, *31*, 2007564.
[53] K. Li, J. Zhang, D. Lin, D.-W. Wang, B. Li, W. Lv, S. Sun, Y.-B. He, F. Kang, Q.-H. Yang, L. Zhou, T.-Y. Zhang, *Nat. Commun.* **2019**, *10*, 725.
[54] J. Kruger, S. Begum, *Encycl. Mater. Sci. Technol.* **2016**, 1701.
[55] V. A. Grachev, A. E. Rozen, Y. P. Perelygin, S. Y. Kireev, I. S. Los, A. A. Rozen, *Heliyon* **2018**, *4*, e00731.
[56] C. A. Loto, *Int. J. Adv. Manuf. Technol.* **2017**, *93*, 3567.
[57] R. Mücke, N. Yaqoob, M. Finsterbusch, F. Al-Jaljouli, P. Kaghazchi, D. Fattakhova-Rohlfing, O. Guillon, *J. Mater. Chem. A* **2023**, *11*, 18801.
[58] Z. Chen, T. Du, S. S. Sørensen, R. Christensen, Q. Zhang, L. R. Jensen, O. V. Magdysyuk, M. Diaz-Lopez, M. Bauchy, Y. Yue, M. M. Smedskjaer, *J. Power Sources* **2023**, *553*, 232302.
[59] R. Xu, K. Zhao, *J. Mech. Phys. Solids* **2018**, *121*, 258.
[60] C. Yuan, W. Lu, J. Xu, *Adv. Energy Mater.* **2021**, *11*, 2101807.
[61] M. G. Boebinger, D. Yeh, M. Xu, B. C. Miles, B. Wang, M. Papakyriakou, J. A. Lewis, N. P. Kondekar, F. J. Q. Cortes, S. Hwang, X. Sang, D. Su, R. R. Unocic, S. Xia, T. Zhu, M. T. McDowell, *Joule* **2018**, *2*, 1783.
[62] J. Tippens, J. C. Miers, A. Afshar, J. A. Lewis, F. J. Q. Cortes, H. Qiao, T. S. Marchese, C. V. Di Leo, C. Saldana, M. T. McDowell, *ACS Energy Lett.* **2019**, *4*, 1475.

[63] T. Krauskopf, F. H. Richter, W. G. Zeier, J. Janek, *Chem. Rev.* **2020**, *120*, 7745.
[64] L. A. Feldman, L. C. De Jonghe, *J. Mater. Sci.* **1982**, *17*, 517.
[65] J. Kasemchainan, S. Zekoll, D. Spencer Jolly, Z. Ning, G. O. Hartley, J. Marrow, P. G. Bruce, *Nat. Mater.* **2019**, *18*, 1105.
[66] D. Lu, Y. Shao, T. Lozano, W. D. Bennett, G. L. Graff, B. Polzin, J. Zhang, M. H. Engelhard, N. T. Saenz, W. A. Henderson, P. Bhattacharya, J. Liu, J. Xiao, *Adv. Energy Mater.* **2015**, *5*, 1400993.
[67] F. Sun, L. Duchêne, M. Osenberg, S. Risse, C. Yang, L. Chen, N. Chen, Y. Huang, A. Hilger, K. Dong, T. Arlt, C. Battaglia, A. Remhof, I. Manke, R. Chen, *Nano Energy* **2021**, *82*, 105762.
[68] L. Barroso-Luque, Q. Tu, G. Ceder, *J. Electrochem. Soc.* **2020**, *167*, 020534.
[69] S. Nemat-Nasser, M. Hori, *J. Appl. Phys.* **1987**, *62*, 2746.
[70] L. Porz, T. Swamy, B. W. Sheldon, D. Rettenwander, T. Frömling, H. L. Thaman, S. Berendts, R. Uecker, W. C. Carter, Y.-M. Chiang, *Adv. Energy Mater.* **2017**, *7*, 1701003.
[71] S. K. Das, S. Lau, L. A. Archer, *J. Mater. Chem. A* **2014**, *2*, 12623.
[72] K. Song, D. A. Agyeman, M. Park, J. Yang, Y.-M. Kang, *Adv. Mater.* **2017**, *29*, 1606572.
[73] I. M. Aldous, L. J. Hardwick, *Angew. Chem. Int. Ed.* **2016**, *55*, 8254.
[74] K. Liu, A. Pei, H. R. Lee, B. Kong, N. Liu, D. Lin, Y. Liu, C. Liu, P.-c. Hsu, Z. Bao, Y. Cui, *J. Am. Chem. Soc.* **2017**, *139*, 4815.
[75] H. Yadegari, Q. Sun, X. Sun, *Adv. Mater.* **2016**, *28*, 7065.
[76] W. Zhou, S. Wang, Y. Li, S. Xin, A. Manthiram, J. B. Goodenough, *J. Am. Chem. Soc.* **2016**, *138*, 9385.